Chinese Chemical Letters 36 (2025) 110179

Contents lists available at ScienceDirect

Chinese Chemical Letters

journal homepage: www.elsevier.com/locate/cclet

Modulating single-atom Co and oxygen vacancy coupled motif for selective photodegradation of glyphosate wastewater to circumvent toxicant residue

Jinshu Huang[a,1], Zhuochun Huang[a,1], Tengyu Liu[a], Yu Wen[a], Jili Yuan[b], Song Yang[a], Hu Li[a,*]

[a] State Key Laboratory of Green Pesticide, Key Laboratory of Green Pesticide and Agricultural Bioengineering, Ministry of Education, State-Local Joint Laboratory for Comprehensive Utilization of Biomass, Center for R&D of Fine Chemicals, Guizhou University, Guiyang 550025, China
[b] Department of Polymer Materials and Engineering, College of Materials & Metallurgy, Guizhou University, Guiyang 550025, China

ARTICLE INFO

Article history:
Received 22 February 2024
Revised 3 June 2024
Accepted 25 June 2024
Available online 10 September 2024

Keywords:
Wastewater treatment
Single-atom catalysts
Photothermal catalysis
Pyroelectric effect
Organic pollutants
Oxygen vacancy

ABSTRACT

The typical wastewater treatment is focused on the photocatalytic efficiency in the degradation of organic pollutants, with little attention to the involved selectivity which may correlate with toxicant residues. Herein, an electron localization strategy for specific O_2 adsorption/activation enabled by photothermal/pyroelectric effect and *in situ* constructed active centers of single-atom Co and oxygen vacancy (Co-O_V) on the Co/BiOCl-O_V photocatalyst was developed for photocatalytic degradation of glyphosate (GLP) wastewater of high performance/selectivity. Under full-spectrum-light irradiation, a high GLP degradation rate of 99.8% with over 90% C–P bond-breaking selectivity was achieved within 2 h, while effectively circumventing toxicant residues such as aminomethylphosphonic acid (AMPA). X-ray absorption spectroscopy and relevant characterizations expounded the tailored anchoring of Co single atoms onto the BiOCl-O_V carrier and photothermal/pyroelectric effect. The oriented formation of more $^{\bullet}O_2^-$ on Co/BiOCl-O_V could be achieved with the Co-O_V coupled center that had excellent O_2 adsorption/activation capacity, as demonstrated by quantum calculations. The formed unique Co-O_V active sites could largely decrease the C–P bond-breaking energy barrier, thus greatly improving the selectivity toward the initial C–P bond scission and the activity in subsequent conversion steps in the directional photocatalytic degradation of GLP. The electron localization strategy by *in situ* constructing the coupled active centers provides an efficient scheme and new insights for the low-toxic photodegradation of organic pollutants containing C–X bonds.

Organophosphorus (OP) is widely available in industrial products, mainly including pesticides, flame retardants, and medicines [1-4]. The interference of OP on the human autonomic nervous system will lead to skeletal muscle paralysis and neuronal damage. Also, it causes great damage to the total phosphorus balance in the aquatic environment [2,4]. However, in the catalytic degradation/treatment process of wastewater, OP is often over-oxidized into more stable and more toxic degradation products such as aminomethylphosphonic acid (AMPA) and omethoate, resulting in secondary pollution [3]. Among various OP pesticides, glyphosate (GLP) is one of the most widely used herbicides in the world, and is also the main source of noxious AMPA in sewage [3,5]. It has been shown that GLP and AMPA are associated with human endocrine disorders and acute and chronic toxicity to aquatic species [6-8]. The degradation of GLP generally follows two degradation paths, including (i) the sarcosine path *via* initial C–P bond cleavage to remove the phosphate group and (ii) the AMPA path through initial C–C bond scission to eliminate the carboxyl group, in which the latter produces more persistent and toxic degradation product AMPA [9]. Therefore, how to achieve highly selective removal of phosphate group while degrading GLP efficiently is an important research direction to guide OP degradation in the future. In recent years, many degradation methods for GLP treatment, such as adsorption, biodegradation and advanced oxidation process (AOPs), have been developed and made excellent progress, but rarely with both high efficiency and low residual toxicity [1,2,10,11].

Photocatalysis is one of the important components of AOPs, which realizes the conversion of solar energy to chemical energy

* Corresponding author.
E-mail address: hli13@gzu.edu.cn (H. Li).
[1] These authors contributed equally to this work.

https://doi.org/10.1016/j.cclet.2024.110179
1001-8417/

to provide chemical energy for the treatment of pollutants [12]. Several types of photocatalysts such as TiO_2-, MnO_2-, CeO_2- and sulfides-based materials have been considered to achieve efficient degradation of GLP, with the focus on the construction of heterojunctions, the activity of which is closely correlated with the oriented formation of specific active species (*i.e.*, $^{\bullet}O_2^-$ or $^{\bullet}OH$) [9,13-18]. For instance, carbon-based and MnO_2-containing photocatalysts can orientedly provide $^{\bullet}OH$, while sulfide-based materials can selectively supply $^{\bullet}O_2^-$ to achieve efficient degradation of GLP [14,16,19-21]. It is also worth noting that the GLP degradation selectivity is affected by its adsorption mode with the photocatalyst, to a certain degree [9,13,15]. In this connection, TiO_2-, CeO_2- and metal-organic frameworks-based photocatalysts have been illustrated to implement selective degradation of GLP by optimizing its adsorption mode to produce low-toxic products [9,13,15]. Therefore, the tailored construction of a bifunctional photocatalyst with the capability to exclusively produce specific active species and the optimal adsorption toward the substrate is anticipated to benefit the efficient and toxic-free photodegradation of GLP *via* a desirable pathway.

As one of the promising alternatives for photocatalytic degradation of organic pollutants, bismuth-based materials have excellent visible light absorption performance due to their narrow band gap, and can be modified/optimized by doping, constructing heterojunctions, defect engineering, and crystal plane engineering [22,23]. (i) Metal doping (*e.g.*, Fe, and Mo) can provide a variety of active species (*e.g.*, $^{\bullet}O_2^-$ and $^{\bullet}OH$) to realize efficient degradation of organic pollutants containing C–N and C–O bonds [24,25]. (ii) The construction of heterojunctions (*e.g.*, $BiOBr/Fe_3O_4$ and Bi_2MoO_6/BiOCl) can achieve efficient degradation of organic pollutants (*e.g.*, GLP and dimethoate) [26,27]. (iii) The defect/crystal plane engineering (*e.g.*, BOC-D_IV_{Cl} and BiOCl(001)) can implement efficient cleavage of C–O bonds in organic pollutants (*e.g.*, GLP and refractory aromatic pollutants) by generating specific active species like $^{\bullet}O_2^-$ [28,29]. Overall, it is demonstrated that bismuth-based materials potentially possess the promising capability to selectively produce specific active species such as $^{\bullet}O_2^-$, but likely lack appropriate adsorption centers for high-efficiency treatment of OP wastewater.

In recent years, single-atom catalysts (SACs) have been developed to exhibit photocatalytic specificity (*e.g.*, broadened light-harvesting range and elevated charge separation/transfer efficiency) because of their unique structure and adsorption characteristics [30]. Single atoms are generally stabilized on the solid carrier through strong metal-support interaction (SMSI), making the catalytic performance of SACs (*e.g.*, Fe-SACs, Cu-SACs, and Co-SACs) closely related to their local coordination environment [31,32]. The study of constructing an asymmetric coordination environment for SACs (*e.g.*, $Mn–N_4$, $Ni–N_3$, and $Zn–N_3O$) has disclosed the enhancement in the adsorption capacity of single atoms toward gas molecules (*e.g.*, CO_2, and O_2), which can markedly elevate the photocatalyst activity [33-35]. By adjusting the coordination number of single-atom metals (*e.g.*, Co, Zn, and Ni) with heteroatoms (*e.g.*, N and O), the adsorption capacity of the metal single atoms toward the gas molecules like CO_2 can be effectively modulated, along with the enhanced separation of photogenerated carriers [36-38]. Apart from optimizing the single-atom site itself, defect structures such as oxygen vacancies (O_V) are also able to promote electron transfer processes, stabilize specific intermediates (*e.g.*, peroxymonosulfate), and especially regulate the adsorption and activation of the substrates (*e.g.*, GLP), contributing to the overall improved efficiency of the single-atom photocatalysts (*e.g.*, Co-SACs and Cu-SACs), to some extent [39-45].

In this context, it is very meaningful and desirable to develop a synergistic strategy of generating specific active substances (*i.e.*, $^{\bullet}O_2^-$ and $^{\bullet}OH$) and supplying optimal adsorption sites for enabling the efficient degradation of GLP while achieving pronounced selectivity to effectively get rid of forming toxic intermediates/co-products. Herein, an electron localization protocol was developed for the highly selective and efficient degradation of GLP by *in situ* constructing single-atom Co-O_V active centers on BiOCl (Co/BiOCl-O_V). The strategy could achieve a high GLP degradation rate of 99.8% within 2 h and selective cleavage of the C–P bond (>90%). The introduction of Co single atoms and the accompanying *in-situ* generation of O_V rendered Co/BiOCl-O_V to have a narrower band gap, which enhanced its light absorption capacity and enabled it to generate more electrons for selective activation of O_2 to form $^{\bullet}O_2^-$. The exclusively generated $^{\bullet}O_2^-$ was highly active for the cleavage of the C–P bond in GLP and was the main reason for the oriented degradation of GLP on the Co-O_V active center of the Co/BiOCl-O_V photocatalyst. Notably, non-selective and deep oxidation of GLP could be remarkably alleviated in the present photocatalytic system without forming poisonous co-products like AMPA, which are typically caused by the confusion of free radical types. This electron localization strategy of introducing O_V *in situ* to modulate the coordination environment of single atoms enables the construction of desired active centers with more photo-induced electron polymerization ability to control the bond-breaking mode, and provides a new reference for wastewater treatment through a rapid and low-toxicity transformation route.

Fig. 1a shows the general preparation procedures of Co/BiOCl-O_V, including an initial solvothermal treatment, and the subsequent impregnation and reduction to introduce Co single atoms. For comparison, BiOCl-O_V, Co/BiOCl, and BiOCl catalysts were also prepared to explore the effects of controlling the variables of O_V and Co single atoms. The structure and morphology of the as-prepared photocatalysts were examined by X-ray diffraction (XRD) and electron microscopy (Figs. 1b-g and Figs. S1 and S2 in Supporting information). The XRD pattern of Co/BiOCl-O_V exhibited eight obvious characteristic peaks at 2θ of 12.02°, 24.18°, 25.90°, 32.55°, 33.52°, 40.96°, 46.69° and 58.70°, which could be attributed to the typical tetragonal crystal form (PDF #82–0485) of the component BiOCl, and identified as (001), (002), (101), (110), (102), (112), (200) and (212) crystal plane, respectively. Notably, the typical crystal face diffraction peaks of Co species were not observed for both Co/BiOCl-O_V and Co/BiOCl, indicating the absence of Co nanoparticles. The transmission electron microscope (TEM) image showed that Co/BiOCl-O_V was in nanoparticle structure (Fig. 1c), mainly resulting from the BiOCl-O_V carrier (Fig. S2). High-resolution TEM (HR-TEM) image of the photocatalyst Co/BiOCl-O_V illustrated the lattice fringes of 0.275 nm and 0.325 nm, corresponding to the (110) and (102) crystal planes of the BiOCl component, respectively (Fig. 1d). These results indicated that the introduction of Co did not have a great influence on the crystal morphology of the BiOCl support. The existence of Co single atoms in Co/BiOCl-O_V could be conjectured by an aberration-corrected scanning transmission electron microscope (AC-STEM, Fig. 1e). The elemental mappings of Co/BiOCl-O_V showed that Bi, O, and Cl elements were concentrated or aggregated somehow, while Co elements were evenly and dispersedly distributed on the Co/BiOCl-O_V photocatalyst (Figs. 1f and g). In addition, a small amount of reduced Bi remained in the photocatalyst but could not be detected, due to its ultrasmall particle size or distribution in internal pores [46].

Fig. 2a illustrates the Bi 4f X-ray photoelectron spectroscopy (XPS) diagrams of Co/BiOCl-O_V, Co/BiOCl, BiOCl-O_V, and BiOCl, and two peaks at 164.5 eV and 159.2 eV corresponded to Bi $4f_{5/2}$ and Bi $4f_{7/2}$, respectively [47-49]. In the O 1s XPS spectra (Fig. 2b), the Co/BiOCl-O_V exhibited two peaks at 531.5 eV and 529.9 eV which were ascribed to O–H and Bi-O, respectively. The binding energies of Bi 4f and O 1s in Co/BiOCl-O_V shifted upward, compared to BiOCl-O_V (Figs. 2a and b), indicating that Bi and O atoms were distinctly affected by the strong electron-withdrawing feature of the

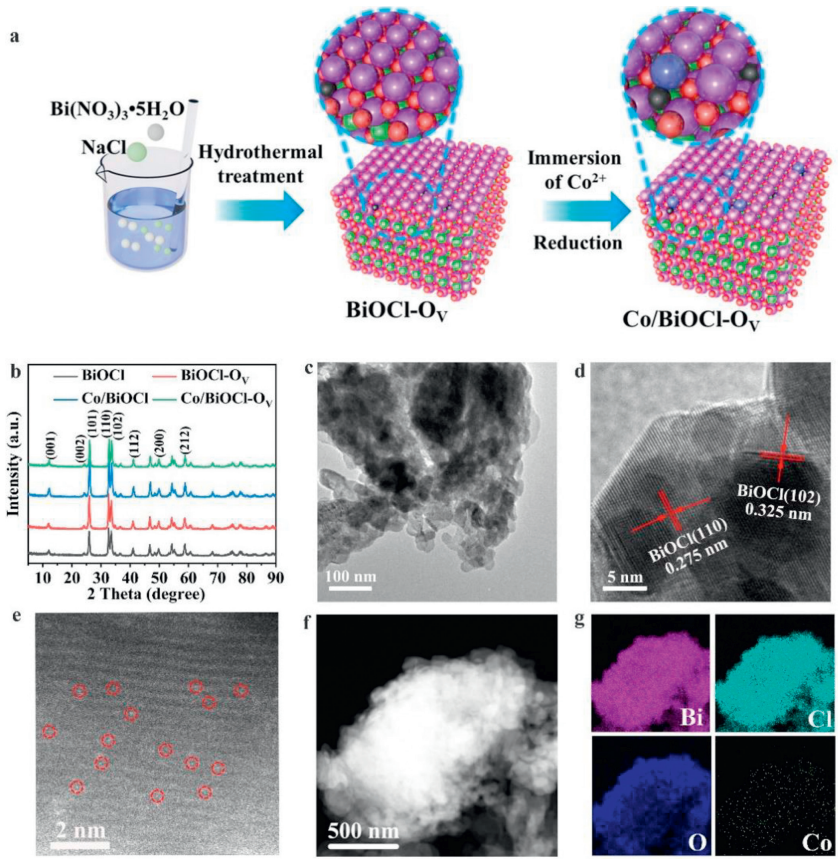

Fig. 1. Construction and structural/morphological characterization of the photocatalysts. (a) The schematic diagram for preparing Co/BiOCl-O_V. (b) XRD patterns of Co/BiOCl-O_V, Co/BiOCl, BiOCl-O_V, and BiOCl. (c) TEM image, (d) HR-TEM image, (e) AC-STEM image, (f) HAADF-STEM image, and (g) the corresponding elemental mappings of Co/BiOCl-O_V.

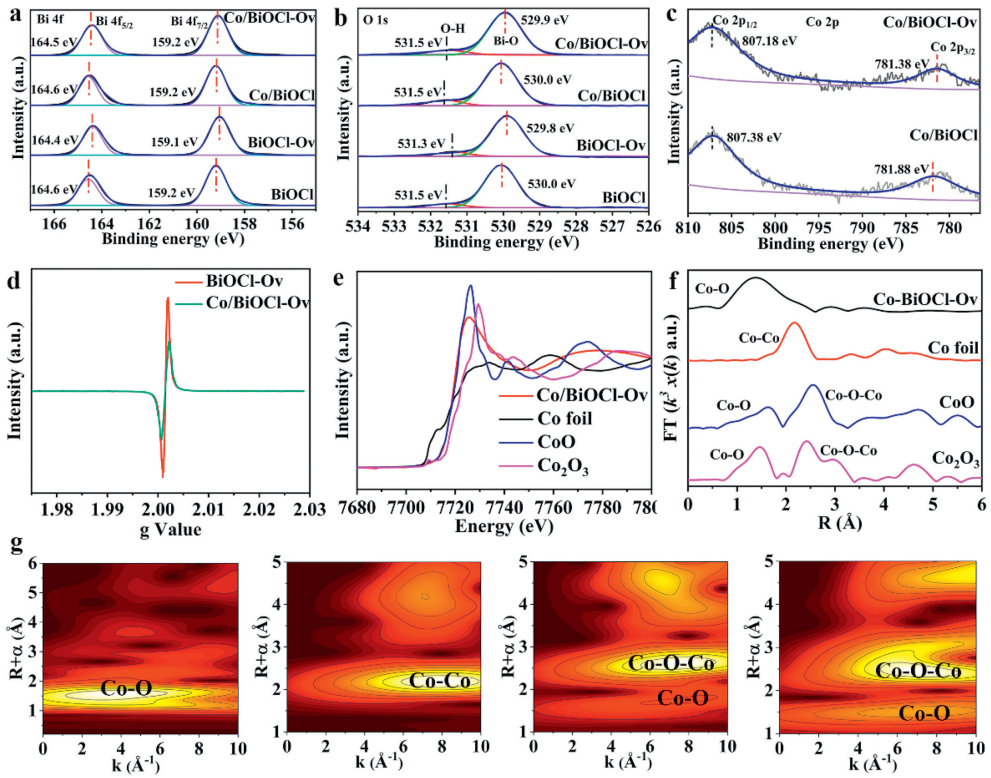

Fig. 2. (a) Bi 4f XPS spectra of Co/BiOCl-O_V, Co/BiOCl, BiOCl-O_V, and BiOCl. (b) O 1s XPS spectra of Co/BiOCl-O_V, Co/BiOCl, BiOCl-O_V, and BiOCl. (c) Co 2p XPS spectra of Co/BiOCl-O_V and Co/BiOCl. (d) EPR spectra of Co/BiOCl-O_V. (e) XANES spectra of Co-foil, CoO, Co_2O_3 and Co/BiOCl-O_V. (f) EXAFS spectra of Co-foil, CoO, Co_2O_3 and Co/BiOCl-O_V. (g) Wavelet-transformed EXAFS spectra of Co-foil, CoO, Co_2O_3 and Co/BiOCl-O_V.

Co elements. In addition, the two XPS fitting peaks of Co/BiOCl-O_V at 807.2 eV and 781.4 eV were attributed to Co $2p_{1/2}$ and Co $2p_{3/2}$, respectively (Fig. 2c). In contrast, the two Co 2p XPS peaks of Co/BiOCl at 807.38 eV and 781.88 eV tended to transfer toward the low binding energy. This strong electron transfer trend between Co single atoms and BiOCl is due to the SMSI [31,32]. In this connection, the electron flow direction in the Co/BiOCl-O_V photocatalyst can be illustrated, that is, the electrons in the BiOCl component of Co/BiOCl-O_V are first gathered in the O_V and then transfer to the single-atom Co sites. The introduction of the Co element makes the binding energy shift of BiOCl in the XPS spectra (Figs. 2a-c), which may be directly related to the change in the Co/BiOCl-O_V structure. Furthermore, the effect of the introduced Co single atoms on the formation of O_V on Co/BiOCl-O_V was investigated by electron paramagnetic resonance (EPR, Fig. 2d). The results showed that the content of O_V greatly increased after Co was loaded onto BiOCl-O_V [50]. The impregnation and reduction method used for introducing Co single atoms is likely to replace the Bi atoms of BiOCl [49], resulting in the generation of O_V *in situ* to form a Co-O_V active center on the photocatalyst Co/BiOCl-O_V.

Further, the valence state of the Co species was studied by X-ray absorption near edge structure (XANES) (Fig. 2e). The Co absorption K-edge of Co/BiOCl-O_V was found between Co foil and CoO, indicating the oxidation state of $Co^{\delta+}$ in the range of $0 < \delta < 2$ (Fig. S3 in Supporting information). Meanwhile, the coordination environment of Co was examined by extended X-ray absorption fine structure (EXAFS) and wavelet-transformed EXAFS (Figs. 2f and g). As shown in Fig. 2f, the dominant peak at 1.99 Å could be attributed to the presence of the Co–O bond of Co/BiOCl-O_V (coordination number: *ca.* 4.1), and no other peaks belonging to *e.g.*, Co–Co and Co–O–Co bonds were detected, suggesting that the Co species might replace the Bi atom in the form of a single atom and was implanted in the BiOCl carrier and coordinated with about four O atoms. Only the intensity change value at *ca.* 1.99 was observed from the wavelet-transformed contour map of Co/BiOCl-O_V (Fig. 1g), indicating that only Co-O bond existed in the Co/BiOCl-O_V photocatalyst, almost without other Co bonding forms. Combined with the results of AC-STEM (Fig. 1e), it could be concluded that Co single atoms were loaded on the Co/BiOCl-O_V photocatalyst in the form of Co–O connection, which could simultaneously lead to the distortion of the carrier lattice, resulting in the generation of more O_V. Overall, it is indicated that the introduction of Co single atoms onto BiOCl is able to effectively produce *in situ* the Co-O_V surface active region, which is consistent with the results of the above XPS spectra (Figs. 2a-c).

It has been reported that the introduction of single atoms will inevitably lead to the efficient separation of photogenerated carriers [31,36,38]. Given this, optical characterizations of the developed photocatalysts were carried out. The behavior of photogenerated carriers was assessed by analyzing the photoluminescence (PL) spectra, photocurrent-time response spectra, and electrochemical impedance spectra (EIS). As shown in Fig. 3a, the PL intensity of Co/BiOCl-O_V, Co/BiOCl and BiOCl-O_V was all relatively lower than that of BiOCl, especially Co/BiOCl-O_V. It is revealed that the introduction of Co atoms and the generation of O_V increased the photo-induced carrier separation, and could be further strengthened by their synergistic effect. The photocurrent-time response and EIS spectra showed that Co/BiOCl-O_V had stronger optical activity (Fig. 3b and Fig. S5 in Supporting information), in agreement with the above PL results. The band positions of Co/BiOCl-O_V, Co/BiOCl, BiOCl-O_V, and BiOCl were calculated based on the data obtained from ultraviolet-visible diffuse reflectance spectroscopy (UV–vis DRS, Fig. 3c), Tauc plots (Fig. 3d), and valence band X-ray photoelectron spectroscopy (VB-XPS, Fig. 3e) spectra. The band gaps of Co/BiOCl-O_V, Co/BiOCl, BiOCl-O_V, and BiOCl were determined to be 3.30 V, 3.39 V, 3.42 V, and 3.50 V, with the valence band (VB) positions at 1.30 V, 1.28 V, 1.48 V, and 1.40 V, respectively. Accordingly, the conduction band (CB) positions of Co/BiOCl-O_V, Co/BiOCl, BiOCl-O_V, and BiOCl could be obtained as −2.00 V, −2.11 V, −1.94 V and −2.10 V, respectively. Based on these data the energy band structure diagrams of the four photocatalysts are shown in Fig. 3f. It can be found that the CB position of BiOCl-O_V with O_V shifted positively, compared with pure BiOCl. Additionally, the VB position of BiOCl after loading with Co single atoms (Co/BiOCl) shifted negatively. Interestingly, Co/BiOCl-O_V was found to bear both features (*i.e.*, CB: −2.00 eV, and VB: 1.30 eV), exhibiting a relatively smaller band gap (Fig. 3f). The improvement in the band structure of Co/BiOCl-O_V could boost its ability to absorb visible light and facilitate the transfer of photogenerated electrons from the VB to the CB, which may significantly improve its photocatalytic activity [51,52]. In addition, it can be speculated from the energy band structure diagrams in Fig. 3f that Co/BiOCl-O_V, Co/BiOCl, BiOCl-O_V, and BiOCl do not have the ability to generate $^{\bullet}OH$ on the VB by capturing electrons from the H_2O molecule, but can satisfy the supply of electrons toward the CB for oriented activation of O_2 to $^{\bullet}O_2^-$. The unique optical properties of Co/BiOCl-O_V are more prone to allow the formation of specific reactive oxygen species (*i.e.*, $^{\bullet}O_2^-$) from O_2 that can be *in situ* generated by water oxidation and endow its enhanced photocatalytic activity for selective degradation of GLP to get rid of generating toxic co-products (*e.g.*, AMPA).

Fig. 3g collects the local temperature variation maps of Co/BiOCl-O_V, BiOCl-O_V, and BiOCl in the time range of 0–6 min visualized by infrared thermal imaging. The local temperature of the Co/BiOCl-O_V system was found to increase from 24.3 °C to 79.8 °C with the irradiation time prolonging from 0 min to 6 min, and the heating rate was 9.2 °C/min. In contrast, the local temperature of BiOCl-O_V and BiOCl increased from 24.3 °C to 65.5 °C and 68.5 °C after the identical irradiation time, with the heating rate of 6.8 °C/min and 7.3 °C/min, respectively. These results showed that the introduced O_V would reduce the photothermal performance of BiOCl-O_V, compared with BiOCl, while the further introduction of Co single atoms could overcome this shortcoming, exhibiting greatly improved photothermal performance. The temperature variation and potential distribution of Co/BiOCl-O_V after 0–6 min were further simulated by COMSOL Multiphysics. According to the pyroelectric theory, the change of pyroelectric potential (U) of the Co/BiOCl-O_V photocatalyst with ΔT can be expressed as follows.

$$U = \frac{P \cdot \Delta T \cdot l}{\varepsilon} \quad (1)$$

where l is the particle size of Co/BiOCl-O_V, ΔT represents the temperature difference and ε is the dielectric constant. The COMSOL simulation results are shown in Fig. 3h. The local temperature of Co/BiOCl-O_V was 24 °C without light irradiation, and the simulated system temperature reached 72 °C in 6 min, which is consistent with the test results of infrared thermal imaging (Fig. 3g). At the same time, the thermopower of the Co/BiOCl-O_V photocatalyst reached 3.2 V after 6 min of irradiation. These simulation results indicated that Co/BiOCl-O_V was subjected to a photothermal effect that could result in a pyroelectric effect and thus release surface charge [53,54]. The pyroelectric effect was reported to promote the separation of photogenerated charges [54], which is more likely beneficial to improve the photocatalytic performance of Co/BiOCl-O_V.

The photocatalytic degradation of GLP with Co/BiOCl-O_V and other as-prepared photocatalysts was conducted to examine the role of the *in situ* electron localization effect enabled by Co-O_V active centers in selective C–P bond cleavage. GLP degradation rates of the tested photocatalysts within 60 min were monitored (Fig. 4a), and Co/BiOCl-O_V showed the highest photocatalytic removal activity of GLP, increasing from 41.2% to 86.1% during the treatment

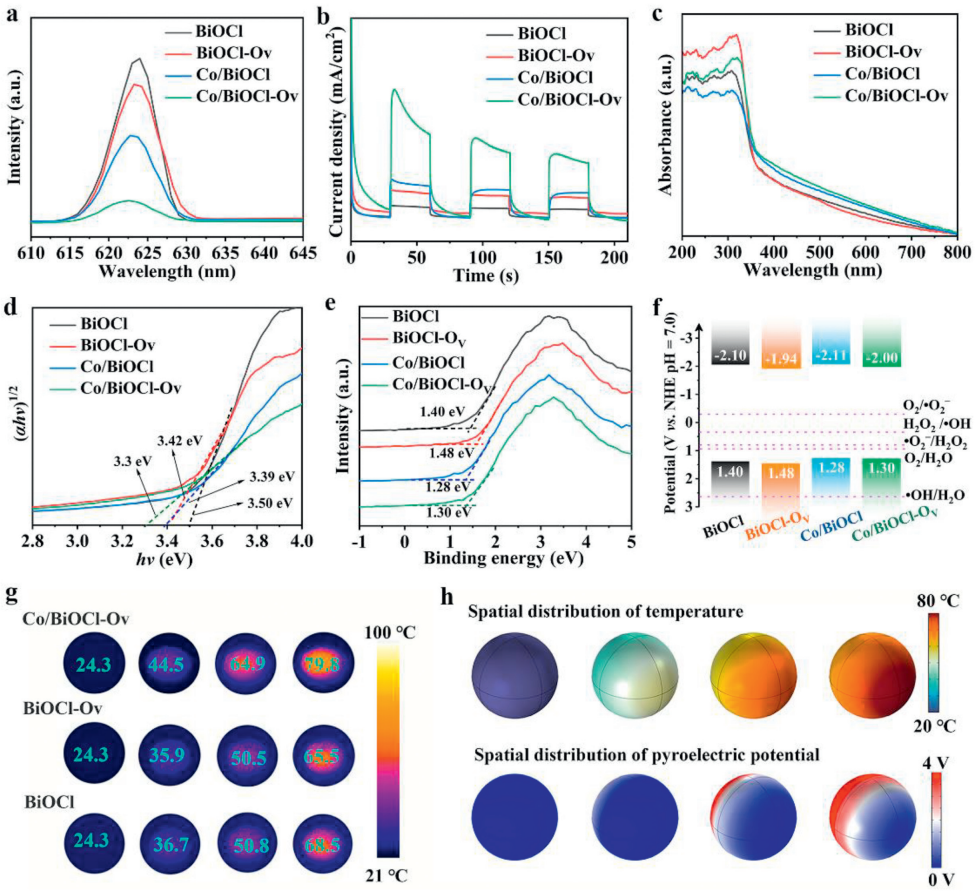

Fig. 3. Characterization of the optical and photothermal/photoelectric properties of as-prepared photocatalysts. (a) PL spectra of Co/BiOCl-O_V, Co/BiOCl, BiOCl-O_V, and BiOCl. (b) Photocurrent-time response spectrum of Co/BiOCl-O_V, Co/BiOCl, BiOCl-O_V, and BiOCl. (c) UV–vis DRS spectra of Co/BiOCl-O_V, Co/BiOCl, BiOCl-O_V, and BiOCl. (d) Tauc plots of Co/BiOCl-O_V, Co/BiOCl, BiOCl-O_V, and BiOCl. (e) VB-XPS spectra of Co/BiOCl-O_V, Co/BiOCl, BiOCl-O_V, and BiOCl. (f) Energy band position diagrams of Co/BiOCl-O_V, Co/BiOCl, BiOCl-O_V, and BiOCl. (g) Infrared thermal images of Co/BiOCl-O_V, BiOCl-O_V, and BiOCl after 0, 2, 4, and 6 min. (h) COMSOL simulations of pyroelectric potential at different temperatures over Co/BiOCl-O_V.

period of 10 min to 60 min. In sharp contrast, inferior degradation rates of 76.2%, 73.7%, and 71.5% were observed for Co/BiOCl, BiOCl-O_V, and BiOCl after 60 min, respectively. Through kinetic fitting of the photocatalytic GLP degradation data after 10–60 min (Fig. 4b), the resulting curves all conformed to the first-order kinetics, with a correlation coefficient (R^2) of greater than 0.99. The apparent rate constants of Co/BiOCl-O_V, Co/BiOCl, BiOCl-O_V, and BiOCl were found to be 0.0288 min^{-1}, 0.0254 min^{-1}, 0.0204 min^{-1}, and 0.0179 min^{-1}, respectively. Upon further extension of the treatment time from 60 min to 120 min, the photocatalytic GLP removal rate of Co/BiOCl-O_V, Co/BiOCl, BiOCl-O_V, and BiOCl could increase to 99.8%, 89.2%, 83.8%, and 78.5%, respectively (Fig. 4c). The relatively faster degradation kinetics and higher degradation rate of Co/BiOCl-O_V are in line with the results of the pronounced optical performance (Figs. 3a and b), also demonstrating the negligible role of reduced Bi residual in BiOCl-O_V. In addition, the influence of different pH and substrate concentrations on the photocatalytic degradation activity of Co/BiOCl-O_V was also collected (Figs. 4d and e), with the aim of screening out the optimal reaction conditions. When the pH increased from 3 to 11, the photocatalytic degradation rate of GLP slightly decreased from 99.9% to 93.5% (Fig. 4d), indicating that the photocatalytic performance of Co/BiOCl-O_V was the best under relatively acidic conditions and not sensitive to the used aqueous media, to a large extent, suggesting the practical application of Co/BiOCl-O_V in GLP wastewater. When the initial concentration of GLP rose from 1 mmol/L to 15 mmol/L, the photocatalytic removal rate was almost constant, to a certain degree (Fig. 4e), indicating the potential feasibility of Co/BiOCl-O_V for real environmental remediation of GLP in variable and even quite low concentrations. It is worth noting that the reactive sites of the Co/BiOCl-O_V photocatalyst might be slightly poisoned by the competitive adsorption/activation of water with GLP in a large amount [55-57].

To untangle the main active species involved in the photocatalytic degradation of GLP, different scavengers were separately added to the photocatalytic reaction solutions with Co/BiOCl-O_V (Fig. 4f), in which ethylenediaminetetraacetic acid (EDTA), silver nitrate ($AgNO_3$), benzoquinone (BQ), and isopropanol (IPA) can be used as the scavenger of hole (h^+), electron (e^-), superoxide radical ($^{\bullet}O_2^-$), and hydroxyl radical ($^{\bullet}OH$), respectively. It was found that the addition of BQ and $AgNO_3$ had the greatest effect on the reaction, and the degradation rate of GLP decreased to 22% and 24%, respectively (Fig. 4f). After the introduction of EDTA, the GLP degradation rate was slightly reduced to 75%, while the presence of IPA had little impact on the degradation activity (94.1%). The results demonstrated that $^{\bullet}O_2^-$ and e^- were the predominant active species in the photocatalytic degradation of GLP. Electron spin resonance (ESR) spectra expounded that under visible light irradiation, Co/BiOCl-O_V had a stronger $^{\bullet}O_2^-$ response than Co/BiOCl, BiOCl-O_V, and BiOCl, and did not show $^{\bullet}OH$ response (Figs. 4g and h), which could well explain the rapid degradation kinetics of GLP over Co/BiOCl-O_V (Fig. 4b). In order to uncover the action causes of the active species, the temperature-programmed desorption of oxygen (O_2-TPD) study was implemented and found that Co/BiOCl-

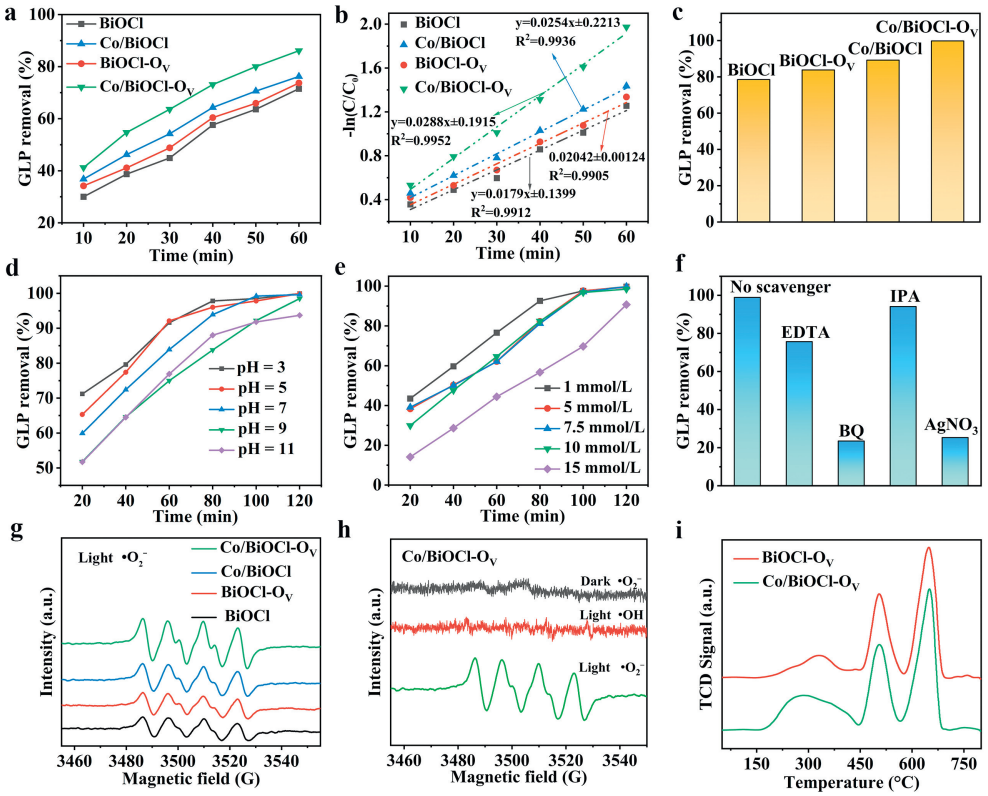

Fig. 4. Investigations on the photocatalytic degradation activity of glyphosate (GLP) wastewater. (a) GLP removal curves, (b) degradative kinetic curves, and (c) GLP degradation rate histograms after 120 min over Co/BiOCl-O_V, Co/BiOCl, BiOCl-O_V, and BiOCl (Reaction conditions: 30 mg catalyst, 7.1 mmol/L initial concentration of GLP, 300 W xenon lamp irradiation, pH 7). The effect of pH (d) and initial concentration of GLP (e) on the photocatalytic degradation rate over Co/BiOCl-O_V, Co/BiOCl, BiOCl-O_V, and BiOCl. (f) The degradation rates of GLP with the introduction of different scavengers after irradiation for 120 min. (g) DMPO-$^{\bullet}O_2^-$ ESR spectra of Co/BiOCl-O_V, Co/BiOCl, BiOCl-O_V, and BiOCl. (h) DMPO-$^{\bullet}$OH ESR and DMPO-$^{\bullet}O_2^-$ ESR spectra of Co/BiOCl-O_V. (i) O_2-TPD curves of Co/BiOCl-O_V and BiOCl-O_V.

O_V had better chemical oxygen adsorption capacity than BiOCl-O_V (Fig. 4i), which may be due to the introduction of Co single atoms that dramatically increase the content of O_V. In this context, the lattice defects formed by replacing Bi atoms with Co single atoms during the photocatalyst preparation process (Figs. 2e-g) could not only facilitate the *in situ* generation of O_V on BiOCl-O_V, but also exactly construct the active center by involving Bi atoms as the core to the active region of Co-O_V (Figs. 2f and g). Overall, the newly tailored Co-O_V active center with appropriate energy band structure (Fig. 3f) was illustrated to have excellent O_2 adsorption and activation capacity (Fig. 4i) for exclusively producing more $^{\bullet}O_2^-$ (Fig. 4h), which could be the reason why Co/BiOCl-O_V exhibited superior photocatalytic activity in GLP degradation (Figs. 4a and c).

The density of states (DOS) is often used to study the electronic structure of the developed catalytic materials. Compared with pure BiOCl (Fig. 5a), the introduction of single-atom Co was found to introduce a doping level in Co/BiOCl, which makes the electronic transition easier (Fig. 5b). The Co-O_V active centers constructed on Co/BiOCl-O_V could shorten the band gap of the photocatalyst while introducing more doping levels caused by the interaction between Co and O_V (Fig. 5c). This could explain why Co/BiOCl-O_V showed a stronger electron transport ability than Co/BiOCl and BiOCl, which is consistent with the result of energy band positions (Fig. 3f) [39]. The electronic structure change of Co/BiOCl-O_V made it show a stronger adsorption capacity for oxygen (Fig. 5d). The adsorption energies (E_{ads}) of O_2 on BiOCl, Co/BiOCl, and Co/BiOCl-O_V were –0.533 eV, –0.871 eV, and –1.553 eV, respectively, which is in accordance with the O_2-TPD results (Fig. 4i). In sum, the Co-O_V active centers *in situ* formed by the introduction of Co single atoms can change the electronic structure of the Co/BiOCl-O_V photocatalyst, which is more conducive to the adsorption and activation of O_2 to give $^{\bullet}O_2^-$ for the enhanced GLP degradation.

In the typical C–P bond-breaking pathway, GLP is first degraded to sarcosine (*m/z* 90.0) and phosphate ions, and then sarcosine is converted to glycine (*m/z* 73.0). Further oxidation of glycine furnishes acetic acid (*m/z* 62.0), glyoxylic acid *m/z* 98.9), and glycolic acid (*m/z* 76.0). For the C–C bond-breaking pathway, GLP is to give toxic degradation product AMPA (*m/z* 111.0). More seriously, studies have shown that the C–P bond of AMPA is extremely inert and therefore difficult to be further mineralized into PO_4^{3-} (Fig. 5e) [3]. To our delight, the photocatalytic GLP degradation was found to dominantly undergo the C–P breaking pathway (over 90% selectivity) rather than the C–C breaking pathway, according to the GLP degradation products detected by LC-MS/MS (Fig. 5f and Fig. S6 in Supporting information).

To further explore the GLP degradation activity and bond-breaking selectivity catalyzed by Co/BiOCl-O_V, the Gibbs free energy evolution of GLP degradation through the C–C bond cleavage and C–P bond cleavage pathways was studied (Fig. 5g). From the results of theoretical calculations, the initial C–P breaking pathway has a relatively lower energy barrier than the C–C breaking pathway. This energy barrier appears in the step of superoxide radical attacking GLP (IS1 to IS2), and the free energy values are 0.37 eV and 0.65 eV for the C–P and C–C breaking pathways, respectively (Fig. 5g). It is indicated that Co/BiOCl-O_V has excellent selectivity of C–P bond breaking of GLP. In the subsequent two spontaneous reaction steps on Co/BiOCl-O_V (IS2 to IS4), it is worth mentioning that the C–P bond cleavage step (IS3 to IS4) of sarcosine (Sar) has a free energy difference of 0.95 eV, while the free energy threshold in the C–C bond cleavage of [(methylamino)methyl]phosphonic

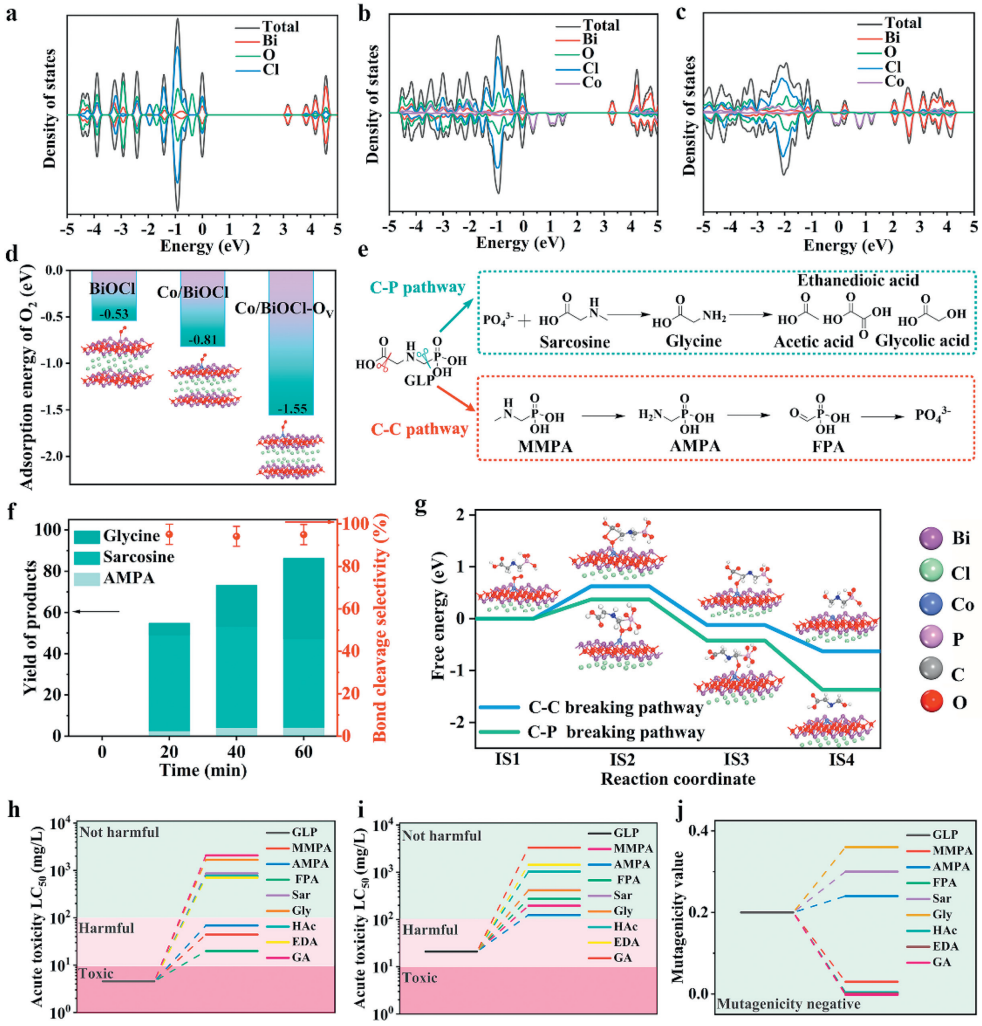

Fig. 5. Study on the mechanism of photocatalytic degradation of glyphosate. The density of states (DOS) for BiOCl (a), Co/BiOCl (b), and Co/BiOCl-O_V (c). (d) The adsorption energy diagrams of O_2 on Co/BiOCl-O_V, Co/BiOCl, and BiOCl. (e) Two pathways of glyphosate (GLP) degradation based on LC-MS analysis. (f) Free energy diagrams of C–C bond and C–P bond breaking of GLP on Co/BiOCl-O_V. (g) The selectivity of the two GLP degradation paths and the distribution of the main products after varying time. Fathead minnow LC_{50} (h), *D. magna* LC_{50} (i), and mutagenicity (j) of GLP and degradation intermediates. MMPA: [(methylamino)methyl]phosphonic acid; AMPA: aminomethylphosphonic acid; FPA: formylphosphonic acid; Sar: sarcosine; Gly: glycine; HAc: acetic acid; EDA: ethanedioic acid; GA: glycolic acid.

acid (MMPA) is only 0.51 eV. The above calculation results explicitly indicate that the initial C–P bond cleavage pathway has higher selectivity in photocatalytic GLP degradation than the initial C–C bond cleavage pathway in the presence of Co/BiOCl-O_V.

Through the characterizations and subsequent DFT calculations, the whole process of GLP degradation on Co/BiOCl-O_V through efficient and selective degradation can be elucidated. Under the excitation of light, due to the SMSI effect between Co single atoms and BiOCl-O_V, the constructed Co-O_V active centers aggregate photogenerated electrons from the BiOCl carrier. This electron localization effect enhances the adsorption capacity of Co/BiOCl-O_V for O_2 (Fig. 5d). The Co-O_V active centers enhance the ability to activate O_2, so that Co/BiOCl-O_V can provide more $^{\bullet}O_2^-$ for photocatalytic degradation of GLP (Figs. 4g and h). The specific active sites and the large amount of $^{\bullet}O_2^-$ produced make the initial C–P bond breaking pathway have a lower energy barrier than the initial C–C bond breaking pathway, thereby achieving highly selective C–P bond scission of GLP (Fig. 5g). This is the main reason why GLP can undergo efficient and selective degradation on Co/BiOCl-O_V, while significantly circumventing the formation of toxic co-product AMPA.

Furthermore, the acute toxicity and mutagenicity of GLP and its degradation products formed through two reaction pathways were evaluated using the quantitative structure-activity relationship (QSAR) method with the toxicity assessment software tool (T.E.S.T.). As shown in Fig. 5h, the LC_{50} (lethal concentration 50) of fathead minnow to die after 96 h was 4.54 mg/L for GLP, which can be classified as "Toxic" (Fig. 5h). The LC_{50} values of Sar, glycine (Gly), acetic acid (HAc), ethanedioic acid (EDA), and glycolic acid (GA) products obtained through the C–P cleavage pathway were all higher than 100 mg/L, which are classified as "Not harmful". In contrast, the degradation products (MMPA, AMPA, and formylphosphonic acid (FPA)) *via* the C–C bond-breaking pathway are classified as "Harmful". It is clearly demonstrated that the GLP degradation products of the C–P bond cleavage pathway have much lower toxicity than that of the C–C bond cleavage pathway. In addition, the LC_{50} of Daphnia magna to die after 48 h was 20.90 mg/L for GLP, which can be categorized as "Harmful". The C–C/C–P degradation products of GLP were all "Not harmful", indicating that the degradation products of GLP in the Co/BiOCl-O_V photocatalytic degradation system were all low-toxic to Daphnia magna (Fig. 5i). Furthermore, it can be seen from Fig. 5j that the mutagenicity of all

degradation products (including GLP) was negative. The QSAR analysis of obtained products in the photocatalytic degradation with Co/BiOCl-O_V showed that the C–P bond cleavage pathway of GLP achieved more low-toxic degradation, while the degradation products of the C–C bond cleavage pathway were still harmful to organisms. Therefore, the high C–P bond cleavage selectivity of Co/BiOCl-O_V in the degradation of GLP makes the developed photocatalytic system have low toxicity and harmless application prospects.

In summary, a novel strategy based on the electron localization effect was developed to *in situ* construct the Co-O_V active centers on Co/BiOCl-O_V for the specific adsorption and activation of O_2, achieving the efficient degradation of GLP with high selectivity toward a low-toxicity conversion pathway. The interaction between Co single atoms and the BiOCl-O_V carrier remarkably facilitated the generation of Co-O_V active centers and embedding single-atom Co into the BiOCl lattice could reduce the coordination number of Co–O connection. Under full-spectrum-light irradiation enabled by photothermal/pyroelectric effect, an excellent GLP degradation rate of 99.8% was obtained over Co/BiOCl-O_V after 2 h, with a high selectivity (>90%) in C–P bond cleavage of GLP that was facilitated by the Co-O_V active centers. The synergy of Co single atoms and O_V was demonstrated to reduce the photocatalyst band gap while introducing more doping levels. O_V could provide more aggregated electrons for single-atom Co active sites and reduce the adsorption energy of O_2. In addition, theoretical calculations expounded that the Co-O_V active centers could markedly reduce the C–P bond-breaking energy barrier and enhance the GLP degradation efficiency and selectivity to significantly circumvent the formation of toxic co-product AMPA. This selectivity-control protocol opens up a new avenue for sewage treatment in a low-toxicity degradation way, and shows great potential in photocatalytic degradation/upcycling of organic pollutants.

Declaration of competing interest

The authors declare that they have no known competing financial interests or personal relationships that could have appeared to influence the work reported in this paper.

CRediT authorship contribution statement

Jinshu Huang: Writing – original draft, Validation, Software, Methodology, Investigation, Conceptualization. **Zhuochun Huang:** Writing – original draft, Validation, Investigation. **Tengyu Liu:** Software. **Yu Wen:** Formal analysis. **Jili Yuan:** Formal analysis. **Song Yang:** Formal analysis. **Hu Li:** Writing – review & editing, Supervision, Methodology, Funding acquisition, Conceptualization.

Acknowledgments

The work was supported by the National Natural Science Foundation of China (No. 22368014), Guizhou Provincial S&T Project (Nos. GCC[2023]011, ZK[2022]011), and Guizhou Provincial Higher Education Institution Program (No. Qianjiaoji[2023]082).

Supplementary materials

Supplementary material associated with this article can be found, in the online version, at doi:10.1016/j.cclet.2024.110179.

References

[1] D. Feng, A. Soric, O. Boutin, Sci. Total Environ. 742 (2020) 140559.
[2] G.K. Sidhu, S. Singh, V. Kumar, et al., Crit. Rev. Env. Sci. Tec. 49 (2019) 1135–1187.
[3] F. Maggi, D. la Cecilia, F.H.M. Tang, et al., Sci. Total Environ. 717 (2020) 137167.
[4] J. Mazuryk, K. Klepacka, W. Kutner, et al., Environ. Sci. Technol. 57 (2023) 9898–9924.
[5] J. Li, Z. Ni, Q. Gao, et al., Chem. Eng. J. 453 (2023) 139972.
[6] G. Andreotti, S. Koutros, J.N. Hofmann, et al., J. Natl. Cancer Inst. 110 (2018) 509–516.
[7] A.H.C. Van Bruggen, M.M. He, K. Shin, et al., Sci. Total Environ. 616-617 (2018) 255–268.
[8] J.C. Mackie, E.M. Kennedy, Environ. Sci. Technol. 53 (2019) 13742–13747.
[9] Y. Huang, Z. Li, K. Yao, et al., Appl. Catal. B 299 (2021) 120671.
[10] P. Garcia-Muñoz, W. Dachtler, B. Altmayer, et al., Chem. Eng. J. 384 (2020) 123315.
[11] X. Chen, F. Liu, B. Liu, et al., J. Hazard. Mater. 287 (2015) 126–132.
[12] Y. Zhang, B. Zhou, H. Chen, et al., Sci. Total Environ. 856 (2023) 159048.
[13] H. Wu, Q. Sun, J. Chen, et al., Chem. Eng. J. 425 (2021) 130640.
[14] D.P. Jaisi, H. Li, A.F. Wallace, et al., J. Agr. Food Chem. 64 (2016) 8474–8482.
[15] L. Gan, M.T. Nord, J.M. Lessard, et al., J. Am. Chem. Soc. 145 (2023) 13730–13741.
[16] Z. Wu, X. He, Y. Xue, et al., Chem. Eng. J. 399 (2020) 125747.
[17] Y.R. Lv, R. Huo, S.-Y. Yang, et al., Sep. Purif. Technol. 197 (2018) 281–288.
[18] X.L. Luo, Z.Y. Chen, S.Y. Yang, et al., J. Colloid Interface Sci. 532 (2018) 456–463.
[19] X. He, Z. Wu, Y. Xue, et al., RSC Adv. 9 (2019) 4635–4643.
[20] Q.Y. Tang, R. Huo, L.Y. Ou, et al., Chinese J. Catal. 40 (2019) 580–589.
[21] Z. Chen, Y. Li, F. Tian, et al., Sep. Purif. Technol. 287 (2022) 120507.
[22] Y. Cheng, Y. Zhang, Z. Wang, et al., Nanoscale 15 (2023) 18571–18580.
[23] H. Li, B. Cheng, J. Zhang, et al., J. Environ. Chem. Eng. 11 (2023) 110371.
[24] T. Zhang, L. Chen, T. Jiang, et al., Mater. Today Commun. 26 (2021) 102145.
[25] Y. Wu, H. Ji, Q. Liu, et al., J. Hazard. Mater. 424 (2022) 127563.
[26] L. Cao, D. Ma, Z. Zhou, et al., Chem. Eng. J. 368 (2019) 212–222.
[27] J. Xue, W. Xiao, L. Shi, et al., J. Environ. Chem. Eng. 11 (2023) 111235.
[28] Y. Sun, W. Han, F. Zhang, et al., Appl. Catal. B 345 (2024) 123689.
[29] Z. Hao, X. Lv, W. Hou, et al., Inorg. Chem. Commun. 134 (2021) 109038.
[30] L. Yang, Z. Chen, Q. Cao, et al., Adv. Mater. 36 (2024) 2306758.
[31] B. Han, Y. Guo, Y. Huang, et al., Angew. Chem. Int. Ed. 59 (2020) 11824–11829.
[32] J. Zhang, C. Liu, B. Zhang, et al., Small Methods 3 (2019) 1800481.
[33] P. Cui, C. Liu, X. Su, et al., Environ. Sci. Technol. 56 (2022) 8034–8042.
[34] X. Zhang, H. Su, P. Cui, et al., Nat. Commun. 14 (2023) 7115.
[35] Y. Li, Y. Guo, G. Fan, et al., Angew. Chem. Int. Ed. 63 (2024) e202317572.
[36] P. Zeng, H. Liu, H. Jia, et al., Appl. Catal. B 340 (2024) 123268.
[37] H. Ou, S. Ning, P. Zhu, et al., Angew. Chem. Int. Ed. 61 (2022) e202206579.
[38] P. Chen, W. Zhang, Y. Sun, et al., Environ. Funct. Mater. 1 (2022) 127–138.
[39] L. Qin, H. Ye, C. Lai, et al., Appl. Catal. B 317 (2022) 121704.
[40] X. Li, T. Han, Y. Zhou, et al., Appl. Catal. B 350 (2024) 123913.
[41] X. Li, Y. Hu, F. Dong, et al., Appl. Catal. B 325 (2023) 122341.
[42] S.S. Shen, X.B. Li, Y.T. Zhou, et al., J. Mater. Sci. Technol. 155 (2023) 148–159.
[43] W. Wang, X. Li, F. Deng, et al., Chin. Chem. Lett. 33 (2022) 5200–5207.
[44] Y. Guo, B. Yan, F. Deng, et al., Chin. Chem. Lett. 34 (2023) 107468.
[45] L. Sun, L. Han, J. Huang, et al., Int. J. Hydrogen Energ. 47 (2022) 17583–17599.
[46] Y. Sun, H. Wang, Q. Xing, et al., Chin. J. Catal. 40 (2019) 647–655.
[47] D.X. Zhao, G.P. Lu, C. Cai, Green Chem. 23 (2021) 1823–1833.
[48] B. Zhang, J. Zhang, R. Duan, et al., Nano Energy 78 (2020) 105340.
[49] C.Y. Wang, Y.J. Zhang, W.K. Wang, et al., Appl. Catal. B 221 (2018) 320–328.
[50] J.J. Ye, P.H. Li, H.R. Zhang, et al., Adv. Funct. Mater. 33 (2023) 2305659.
[51] J. Zhang, P. Sun, Z. Mo, et al., J. Colloid Interf. Sci. 652 (2023) 470–479.
[52] J. Yang, T. Xie, Y. Mei, et al., Appl. Catal. B 339 (2023) 123149.
[53] D. Wang, Y. Liu, Q. Wang, et al., J. Hazard. Mater. 436 (2022) 129224.
[54] M. Li, J. Sun, G. Chen, et al., Adv. Powder Mater. 1 (2022) 100032.
[55] Q. Li, J. Zhang, J. Zhou, et al., Chem. Eng. J. 467 (2023) 143310.
[56] A.J. Martín, S. Mitchell, C. Mondelli, et al., Nat. Catal. 5 (2022) 854–866.
[57] Y. Ying, Z. Lin, H. Huang, ACS Energy Lett. 8 (2023) 1416–1423.